Preprint 19 April 2021

Trajectory Design of Earth-enabled Sun Occultation Missions

N. Bernardini,[1]* N. Baresi,[1] R. Armellin,[2] S. Eckersley[3] and S.A. Matthews[4]
[1]*Surrey Space Centre, University of Surrey, Guildford GU2 7XH, UK*
[2]*Te Punaha - Auckland Space Institute, Institution, Auckland 1010, New Zealand*
[3] *Surrey Satellite Technology Limited, Tycho House, 20 Stephenson Road, Surrey Research Park, Guildford GU2 7YE, UK*
[4] *Mullard Space Science Lab, University College of London, Holmbury St Mary, RH5 6NT, UK*

Accepted XXX. Received YYY; in original form ZZZ

ABSTRACT

Understanding the solar corona and its structure, evolution and composition can provide new insights regarding the processes that control the transport of energy throughout the solar atmosphere and out into the heliosphere. However, the visible emission coming from the corona is more than a million times weaker than the emission from the photosphere, implying that direct corona observations are only possible when the Sun is obscured. The goal of this paper is to perform a feasibility study of a Sun occultation mission using the Earth as an occulter. The challenge is that the occultation zone created by the Earth does not follow a Keplerian trajectory, causing satellites placed in this region to quickly drift apart from the target area. To increase the number of revisits while optimizing the propellant budget, we propose optimal trajectories in the Sun-Earth-Spacecraft circular restricted three body problem that account for scientific and engineering constraints such as limited power budget and mission duration. Chemical propulsion, electric propulsion and solar sailing configurations are compared in terms of performance and mission feasibility, revealing how 24 hours of corona observations would be possible every 39 days with as little as 199 m/s ΔV-equivalent of propellant. The feasibility of the solar sail approach is hereby demonstrated, making it a challenging engineering alternative to currently available technologies.

Key words: Solar Corona – Sun Occultation Mission – Optimal Trajectories – CRTBP – Solar Sailing

1 INTRODUCTION

The corona and solar wind form one of the key elements in controlling planetary environments within the solar system, and indeed the size and shape of the heliosphere itself. At the heart of the origin and evolution of the corona is the solar magnetic field, which is responsible for the organisation of the solar plasma at all scales, and for the storage, transport and release of magnetic energy. Alongside the still poorly understood processes that control both the existence and the large-scale variation of the corona and the acceleration of the solar wind, the corona is also the region of the solar atmosphere where it is believed that the explosive energy release responsible for flares and coronal mass ejections (CMEs) occurs; these are the key drivers of space weather events Boe et al. (2020). Despite the critical role that this region plays in controlling the release of plasma and magnetic field into the heliosphere, measuring the magnetic field responsible remains a significant challenge, hampered by the high plasma temperature and weak intensity in the visible, and until very recently (Si et al. (2020); Landi et al. (2020)), a complete lack of diagnostics in the extreme ultraviolet (EUV). Consequently many of our models rely on the extrapolation of measurements of the photospheric magnetic field and assumptions that the coronal field becomes radial beyond the 'source surface' Altschuler & Newkirk (1969); Schatten et al. (1969). However, recent work by Boe et al. (2020) demonstrates that this assumption is over simplistic and there is substantial inhomogeneity and variation across the solar cycle. This result has significant implications not only for existing models of the coronal magnetic field but also for solar wind acceleration models and the linking of in situ measurements to solar source regions: a central goal of the Solar Orbiter mission Zouganelis et al. (2020).

From the ground, total solar eclipses offer a unique opportunity to observe the corona down to its base and typically at much higher spatial and temporal resolution than routinely possible. However, these events only occur every 18 months on average, lasting typically only for a few minutes Eckersley & Kemble (2017). It was the pioneering work of Lyot (1932) in the development of the coronagraph that made the routine observation of the corona in the visible possible in both broadband continuum and spectral lines. While such observations allow detailed study of the structure and temporal variations of the coronal intensity, and, indirectly the morphology of the coronal magnetic field, work by e.g. Arnaud & Newkirk (1987); Lin et al. (2004); Tomczyk et al. (2007) further opened the possibility to directly infer the strength and direction of the field through polarization measurements.

The concept of the coronagraph instrument is to occult the sun by placing an artificial disk that projects an artificial eclipse on the instrument sensor. This instrument presents some limitations related to the presence of daylight like atmospheric seeing and scattering which limits how close to the solar disk one is able to observe. Space-based observations limit these effects to some degree, in particular atmospheric seeing, and coronagraphs have been key instruments on many solar missions since the 1980s, e.g. the coronagraph and polarime-

* E-mail: n.bernardini@surrey.ac.uk

ter on the Solar Maximum Missions MacQueen et al. (1980) and the LASCO coronagraph on the Solar and Heliospheric Observatory (SOHO) Domingo et al. (1995). However, these instruments are also limited by stray light and vignetting for observations in the lower corona, as a result of the small occulter diameter and subsequent short distance between the occulter and the aperture of the instrument Eckersley & Kemble (2017).

New space missions with larger occulters have recently been proposed to overcome the limitations of current instrumentation suites. ESA's Proba-3 mission, to be launched in mid 2022 Llorente et al. (2013), will study the corona of the Sun via two satellite flying in formation. One satellite, the observer, will fly in a tight formation behind the occulter along the Sun-occulter line of sight. Despite significant engineering challenges associated with operating two satellites in a tight Earth formation, the mission will allow observations lasting 6 hours. An alternative approach is introduced in Eckersley & Kemble (2017), where the use of natural occulting bodies was first proposed.The large distance between the occulter and the observer allows us to have much larger baselines than other conventional coronographs. This would highly limit undesired phenomena like vignetting and straight light effects, improving the observations of the inner corona Eckersley & Kemble (2017). In addition to that the use of a natural occultation zone enables more frequent and longer observations compared to observations performed on Earth.The patent focuses on using the Moon as an occulting body, regardless of strong dynamical perturbations due to the gravitational influence of the Earth. The aim of this paper is to perform a feasibility study of a similar concept, where Earth is used as an occulting body rather than the Moon. While the Earth is less spherical than the Moon and it is possible to have atmospheric effects during the observation, the advantage of using the Earth as occulter is that the target zone remains fixed in the rotating frame of the Sun-Earth system. Accordingly, trajectories are designed in the Sun-Earth circular restricted three-body problem while taking into account the preliminary engineering requirements of a typical small satellite mission (i.e., limited ΔV budget and power capabilities). Focus is given to the definition of two controlled trajectories and their ΔV budgets for bringing the satellite back into the occultation zone. Chemical, low-thrust and solar sail are investigated as possible propulsion systems and compared in terms of time-of-flight and ΔV cost per observation cycle. Optimal control theory and indirect optimization methods are adopted to compute the desired transfers.

This paper is organized as follows: first a definition of the occultation zone and the penumbra is provided, followed by the equations of motion adopted in this study. Two mission profiles are presented in Section 4 along with system parameters adopted for the numerical simulations. The optimal control problem solution methodology is then explained. Main results and conclusions are summarized in the remaining two paragraphs of the manuscript.

2 OCCULTATION ZONE AND PENUMBRA

The occultation zone is a small region found at the edge of the umbra cone created by the Earth. This region can be exploited to perform regular observations of the solar corona as follows.

Neglecting the oblateness of the occulting body, the zone is defined by the tangents to the Sun and the Earth, as shown in Figure 1. It is necessary to identify two Sun radii; the first radius is the reference radius of the Sun ($R_{1\odot}$), while the second ($R_{2\odot}$) identifies field of view. This second radius represents the radius of the corona and it is defined by multiplying the reference radius with

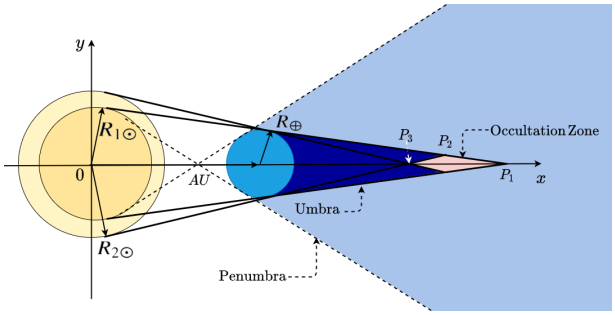

Figure 1. Occultation Zone, Umbra and Penumbra Regions

Symbol	Quantity	Value	Units
$R_{1\odot}$	Sun Radius	6.9555×10^5	km
$R_{2\odot}$	Expanded Sun Radius	7.09461×10^5	km
AU	Sun Earth Distance	1.49598×10^8	km
$R_\oplus$	Earth Radius	6378.137	km
P_1	Right Edge Occultation Zone	$(1.50982 \times 10^8, 0, 0)$	km
P_2	Centre Edge Occultation Zone	$(1.50955 \times 10^8, 0, 0)$	km
P_3	Left Edge Occultation Zone	$(1.5097 \times 10^8, 63.73, 0)$	km

Table 1. Occultation Zone Parameters

an expansion factor. For the observation of the Sun corona a factor of 1.02 is used Eckersley & Kemble (2017) but smaller factor could be achieved adopting the same procedures presented in this study. Similar missions with different field of view have been proposed: Proba-3 is planned to have a field of view 1.08 $R_{1\odot}$ Loreggia et al. (2019), HiRISE proposed field of view is 1.01 $R_{1\odot}$ Erdelyi (2019).

The penumbra region is computed by taking the tangent lines to the Sun and Earth as shown in Figure 1. The amount of solar radiation that the satellite receives while in the penumbra, called shadow factor (τ) is computed as shown in Montenbruck et al. (2002). Using $\mathbf{r_2}$ and $\mathbf{r}_\odot$ as the position of the spacecraft and the Sun w.r.t. the occulting body respectively as shown in Figure 2, the shadow factor is computed as follow:

$$\tau = \begin{cases} \tau = 1 & \text{if } a + b \leqslant c \\ \tau = 0 & \text{if } c \leqslant |b - a| \\ \tau = 1 - \frac{A}{\pi a^2} & \text{otherwise,} \end{cases} \tag{1}$$

where

$$a = \arcsin\left(\frac{R_\odot}{\|\mathbf{r}_\odot - \mathbf{r_2}\|}\right), \tag{2a}$$

$$b = \arcsin\left(\frac{R_\oplus}{\|\mathbf{r_2}\|}\right) \tag{2b}$$

$$c = \arccos\left(-\frac{(\mathbf{r}_\odot - \mathbf{r_2})}{\|\mathbf{r}_\odot - \mathbf{r_2}\|} \cdot \frac{\mathbf{r_2}}{\|\mathbf{r_2}\|}\right), \tag{2c}$$

$$\chi = \frac{c^2 + a^2 - b^2}{2c}, \tag{2d}$$

$$\phi = \sqrt{a^2 - \chi^2}, \tag{2e}$$

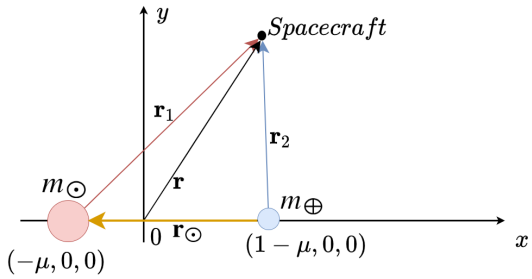

Figure 2. Planar CRTBP coordinates in the rotating frame

$$A = a^2 \arccos\left(\frac{\chi}{a}\right) + b^2 \arccos\left(\frac{c-\chi}{b}\right) c\ \phi. \tag{2f}$$

3 EQUATION OF MOTIONS

Because the occultation zone is found along the position vector of the Earth as seen from the Sun, the problem of designing optimal trajectories from / to the occultation zone can be better investigated in the synodic frame of the Sun-Earth circular restricted three body problem. The frame is centered in the baricenter of the two primaries, the Sun and the Earth, and oriented such that $\hat{\boldsymbol{x}}$ is constantly aligned with the Sun-Earth direction, $\hat{\boldsymbol{z}}$ is perpendicular to the orbital plane of the Earth, and $\hat{\boldsymbol{y}} = \hat{\boldsymbol{z}} \times \hat{\boldsymbol{x}}$ completes the right-handed triad. In this reference frame, the occultation zone remains fixed along the positive $\hat{\boldsymbol{x}}$ axis near $x \simeq 1.00916$ AU. In what follows, the length and time units of the problem are set to 149597870.7 km and 5022635 s, respectively, so that the primaries $m_\odot$ and $m_\oplus$ may be found along the $\hat{\boldsymbol{x}}$-axis in $(-\mu, 0, 0)$ and $(1-\mu, 0, 0)$, respectively. Here, the value of mass ratio parameter, i.e., $\mu = m_\oplus/(m_\oplus + m_\odot)$, is 3.0035×10^{-6}. Furthermore, denoting the state of the satellite as $\mathbf{x} = [\mathbf{r}, \mathbf{v}, m]$, the equations of motions becomes Koon et al. (2008):

$$\dot{\mathbf{x}} = \mathbf{f}(\mathbf{x}) = \begin{cases} \mathbf{v} \\ \mathbf{g}(\mathbf{r}) - 2[\mathbf{z}]\mathbf{v} + \frac{T_{max} u}{m}\boldsymbol{\alpha} \\ -\frac{T_{max} u}{I_{sp} g_0} \end{cases} \tag{3}$$

where

$$\mathbf{g}(\mathbf{r}) = -\frac{1-\mu}{r_1^3}\mathbf{r}_1 - \frac{\mu}{r_2^3}\mathbf{r}_2 - [\mathbf{z}][\mathbf{z}]\mathbf{r}, \tag{4a}$$

$$[\mathbf{z}] = \begin{bmatrix} 0 & -1 & 0 \\ 1 & 0 & 0 \\ 0 & 0 & 0 \end{bmatrix}, \tag{4b}$$

$$r_1 = \sqrt{(x+\mu)^2 + y^2 + z^2}, \tag{4c}$$

and

$$r_2 = \sqrt{(x-1+\mu)^2 + y^2 + z^2}. \tag{4d}$$

Moreover, T_{max} is the maximum thrust, I_{sp} is the specific impulse, $\boldsymbol{\alpha}$ is the satellite control direction and $u \in [0, 1]$ represents the throttle.

Notice that the equations of motion admits an integral of motion known as the Jacobi integral as long as $u = 0$:

$$C = -(\dot{x}^2 + \dot{y}^2 + \dot{z}^2) - 2U(x, y, z), \tag{5}$$

where

$$U(x, y, z) = -\frac{1-\mu}{r_1} - \frac{\mu}{r_2} - \frac{1}{2}\mu(1-\mu) - \frac{1}{2}[\mathbf{z}][\mathbf{z}]\mathbf{r}^T\mathbf{r} \tag{6}$$

is the effective potential consisting of gravitational, constant, and centrifugal terms.

4 CANDIDATE MISSION PROFILES

The occultation zone is 0.00084 length units away from the collinear L2 Lagrangian point, so a satellite placed there would quickly drift away unless properly controlled back to the target area. It is assumed that the satellite can only operate with its own batteries while performing its measurement campaigns. As a result of this assumption, the satellite will be required to exit from the region of penumbra to recharge its batteries before beginning a new cycle. The operational phase can be then divided into two main phases: a ballistic coasting phase and a controlled arc.

The controlled trajectory goes from an initial state, $\mathbf{x}_0$, to a final state, $\mathbf{x}_f$. The initial and final conditions are chosen by imposing a zero velocity passage through the occultation zone and propagating the state forward and backward in time. More specifically we require the satellite velocity to be zero in the rotating frame when aligned with the Sun and Earth:

$$\mathbf{x}_0^{TZ} = \begin{bmatrix} x^{TZ} \\ 0 \\ 0 \\ 0 \\ 0 \\ 0 \end{bmatrix} \tag{7}$$

This particular choice of zero velocity passages ensures that the satellite does not escape the system even if it is uncontrolled as shown in Figure 3. The choice of x^{TZ} is driven by the observation time. As shown in Figure 4, selecting an observation time yields two possible values of x^{TZ} in the occultation zone (one on the left side of the polygon, and one on the right). The numerical simulations presented in this paper focus on the right side of the polygon, although similar investigations could be made for the other point in the target zone. Once a point in the occultation zone has been picked, the initial conditions of the spacecraft are integrated using Equation (3) with $u = 0$ until the satellite leaves the penumbra region. Here, the satellite is left to coast for a certain number of days, depending on the requirement for batteries recharge. At the end of this coasting phase, the state of the spacecraft is fixed and labelled as $\boldsymbol{x}_0$ hereafter. A similar procedure is implemented for the definition of $\mathbf{x}_f$. In this case, $\mathbf{x}_0^{TZ}$ is propagated backward in time until it crosses the occultation zone or the time elapsed reaches a user-defined value. The first scenario is presented in Figure 5 and hereby referred as the propelled scenario. The second case is represented in Figure 6 and it is referred as the solar sail scenario. The names follow from the performances of the different propulsion technologies as shown in Section 6. We note here that a particular case of the solar sail scenario where $\mathbf{x}_0$ and $\mathbf{x}_f$ are symmetric with respect to the x-axis of synodic frame is also analyzed in order to enable battery recharging before and after the controlled leg of the trajectory cycle. In all the cases, an optimal control trajectory from $\mathbf{x}_0$ to $\mathbf{x}_f$ needs to be implemented. Once at $\mathbf{x}_f$ the spacecraft would eventually return to the initial point in the occultation zone and restart its loop.

Considering that observations of the solar corona on ground last only a few minutes and the limitations of batteries capacity, the

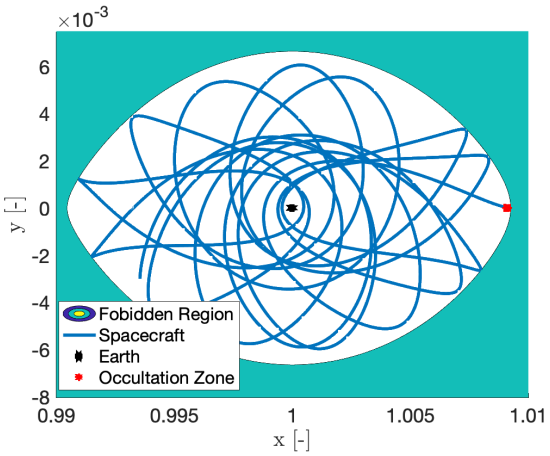

Figure 3. Uncontrolled trajectory starting from $\mathbf{x}_0^{TZ}$.

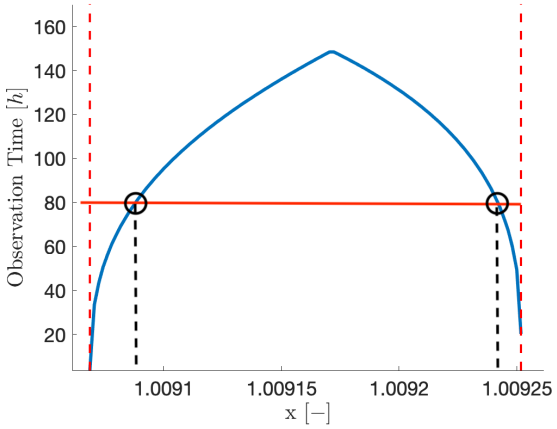

Figure 4. Observation time as a function of x in the occultation zone. Zero-velocity points for an 80-hour observation window are shown as an example.

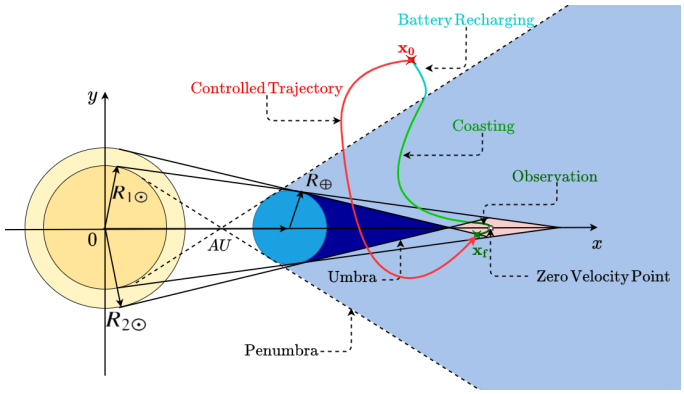

Figure 5. Propelled mission scenario. The spacecraft coasts from the occultation zone until it exits the penumbra region (green), from there it continue coasting while recharging the batteries (cyan) and it is then controlled back to the occultation zone (red trajectory). Note that the figure is only illustrative and not in scale

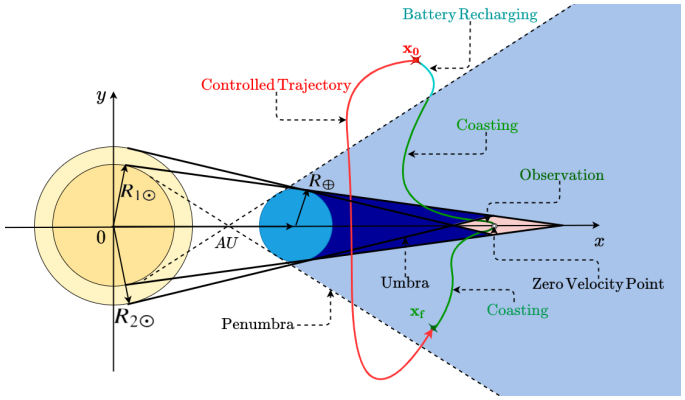

Figure 6. Solar sail scenario. The spacecraft coasts from the occultation zone until it exits the penumbra region (green), from there it continues coasting while recharging the batteries (cyan), it is then controlled back to the final state $\mathbf{x}_f$ and from there it naturally coasts back to the occultation zone (green).

Table 2. Spacecraft reference parameters for the chemical, electric, and solar sail configurations.

Symbol	Quantity	Value	Units
T_{max} Chemical	Max Thrust	1	N
Isp Chemical	Specific Impulse	200	s
T_{max} Low-Thrust	Max Thrust	0.1	N
Isp Low-Thrust	Specific Impulse	2000	s
m_0	Wet Mass	100	kg
u_{max}	Solar Sail Max Acc	1	mm / s^2

time for observations in the occultation zone is fixed to 24 hours. The study is performed considering some typical values for a small satellite system equipped with 3 different propulsion technologies: chemical propulsion, low-thrust propulsion, and solar sailing. The reference values for the spacecraft are shown in Table 2 along with the maximum thrust and specific impulses used for the numerical simulations.

5 OPTIMAL CONTROL PROBLEM

Consider a mass particle subject to the dynamics $\dot{\mathbf{x}} = \mathbf{f}(\mathbf{x}, \mathbf{u}, \mathbf{t})$. The aim of an optimal control problem is to find the control $\mathbf{u}$ that minimizes a performance index J. In this section the methodologies to compute fuel optimal, time optimal and solar sail trajectories are explained.

5.1 Fuel Optimal

The fuel optimal problem is of greatest interest from an engineering point of view since decreasing the fuel mass on a spacecraft means decreasing the price of a mission or increasing its payload capacity. The fuel optimal problem formulation is given below assuming a fixed time of flight ToF $= t_f - t_0$. The cost function is defined from Jiang et al. (2012)

$$J = \lambda_0 \frac{T_{max}}{I_{sp} g_0} \int_{t_0}^{t_f} u \, dt \tag{8}$$

and needs to be minimized subject to:

(i) dynamics constraint, given by Eq. (3);

(ii) initial conditions

$$\boldsymbol{\psi}^0 = \begin{bmatrix} \mathbf{r}_0 - \mathbf{r}(t_0) \\ \mathbf{v}_0 - \mathbf{v}(t_0) \\ m_0 - m(t_0) \end{bmatrix} = 0; \tag{9}$$

(iii) final conditions

$$\boldsymbol{\psi}^f = \begin{bmatrix} \mathbf{r}_f - \mathbf{r}(t_f) \\ \mathbf{v}_f - \mathbf{v}(t_f) \end{bmatrix} = 0. \tag{10}$$

It is possible to define the Hamiltonian of the fuel optimal problem by introducing the Lagrange multipliers (or adjoints) $\boldsymbol{\lambda} = [\boldsymbol{\lambda}_r; \boldsymbol{\lambda}_v; \lambda_m]$. The inclusion of $\boldsymbol{\lambda}$ and its scaling factor λ_0 allows us to reduce the solution of the fuel optimal problem into a well-posed two point-boundary value problem arising from the Hamiltonian:

$$\begin{aligned} H = \lambda_0 \frac{T_{max}}{I_{sp} g_0} u + \boldsymbol{\lambda}_r^T \mathbf{v} + \boldsymbol{\lambda}_v^T \left(\mathbf{g}(\mathbf{r}) - 2\,[\mathbf{z}]\,\mathbf{v} + \frac{T_{max} u}{m} \boldsymbol{\alpha} \right) + \\ - \lambda_m \frac{T_{max}}{I_{sp} g_0} u. \end{aligned} \tag{11}$$

Following Pontryagin's minimum principle, the Hamiltonian can be minimized with respect to the control variables u and $\boldsymbol{\alpha}$ via Lawden's primer vector. It follows that the optimal thrust magnitude that minimizes the Hamiltonian is given by Conway (2010):

$$u = \begin{cases} 0 & if \;\; \rho > 0 \\ 1 & if \;\; \rho < 0 \end{cases}, \tag{12}$$

where ρ is called switching function and it is defined as Jiang et al. (2012):

$$\rho = 1 - \frac{I_{sp} g_0}{m} \frac{\lambda_v}{\lambda_0} - \frac{\lambda_m}{\lambda_0}, \tag{13}$$

and the optimal control direction is given by Conway (2010):

$$\boldsymbol{\alpha} = -\frac{\boldsymbol{\lambda}_v}{\lambda_v}. \tag{14}$$

From the stationary condition of the Hamiltonian it then follows:

$$\frac{\partial H}{\partial \boldsymbol{\lambda}} = \dot{\mathbf{x}} \;\rightarrow\; \dot{\mathbf{x}} = \mathbf{f}\,(\mathbf{x}, \mathbf{u}, t)\,, \tag{15}$$

$$\frac{\partial H}{\partial \mathbf{x}} = -\dot{\boldsymbol{\lambda}} \;\rightarrow\; \begin{cases} \dot{\boldsymbol{\lambda}}_r = -G \boldsymbol{\lambda}_v \\ \dot{\boldsymbol{\lambda}}_v = -\boldsymbol{\lambda}_r + 2[\mathbf{z}]\boldsymbol{\lambda}_v \\ \dot{\lambda}_m = -\frac{T_{max} u}{m^2} \lambda_v \end{cases}, \tag{16}$$

where

$$G = -\frac{1-\mu}{r_1^3} \left(I - 3 \frac{\mathbf{r}_1 \mathbf{r}_1^T}{r_1^2} \right) - \frac{\mu}{r_2^3} \left(I - 3 \frac{\mathbf{r}_2 \mathbf{r}_2^T}{r_2^2} \right) - [\mathbf{z}][\mathbf{z}] \tag{17}$$

is the Hessian of the effective potential. Notice that not all the final conditions are known since the mass of fuel is the value that has to be minimized. Accordingly. the final condition on the mass is substituted by a final condition on the mass adjoint, which must be equal to zero. The initial and final boundary conditions become:

$$\boldsymbol{\phi}_0 = \mathbf{x}_0 - \mathbf{x}(t_0) = 0; \tag{18a}$$

$$\boldsymbol{\phi}_f = \begin{bmatrix} \mathbf{r}_f - \mathbf{r}(t_f) \\ \mathbf{v}_f - \mathbf{v}(t_f) \\ \lambda_m(t_f) \end{bmatrix} = 0. \tag{18b}$$

It is helpful to rewrite the problem with a smooth control profile as done in Rasotto et al. (2016). In this way it is possible to eliminate the discontinuity produced by Equation 12 with the addition of a smoothing factor $k \in (0, \infty)$:

$$u = \frac{1}{1 + e^{2k\rho}}. \tag{19}$$

A good set of initial adjoints is required to solve the fuel optimal control problem as the convergence region is generally small. To choose the initial adjoints for the single shooting method, a particle swarm optimizer is used as recommended in Jiang et al. (2012). Here, the addition of λ_0 becomes relevant in that it reduces the search space of the optimizer to the surface of an 8-dimensional unit sphere such that

$$\|\boldsymbol{\nu}(t_0)\| = 1, \tag{20}$$

where $\boldsymbol{\nu} = [\lambda_0,\; \boldsymbol{\lambda}^T]^T$.

Introducing the optimization variables $[x_1, x_2, x_3, x_4, x_5, x_6, x_7] \in [0, 1]$, one has that the initial adjoints can be defined as

$$\begin{aligned} \lambda_0 &= \sin(\beta_1) \\ \boldsymbol{\lambda}_{r0} &= \cos(\beta_1)\cos(\beta_2)\cos(\beta_3) \times \\ &\quad \times [\cos(\beta_4)\cos(\beta_6)\,; \cos(\beta_4)\sin(\beta_6)\,; \sin(\beta_4)] \\ \boldsymbol{\lambda}_{v0} &= \cos(\beta_1)\cos(\beta_2)\sin(\beta_3) \times \\ &\quad \times [\cos(\beta_5)\cos(\beta_7)\,; \cos(\beta_7)\sin(\beta_7)\,; \sin(\beta_5)] \\ \lambda_{m0} &= \cos(\beta_1)\sin(\beta_2)\,, \end{aligned} \tag{21}$$

where

$$\begin{aligned} \beta_{1,2,3} &= \frac{\pi}{2}\,[x_1; x_2; x_3] \\ \beta_{4,5} &= \pi \left([x_4; x_5] - \frac{1}{2} \right) \\ \beta_{6,7} &= 2\pi\,[x_6; x_7]\,. \end{aligned} \tag{22}$$

Provided with a crude approximation of the initial adjoints obtained with the particle swarm optimizer, the two-point boundary value problem described in this section can be solved iteratively with a single-shooting procedure. Upon convergence, the initial adjoints can be passed as an initial guess for the same two-point boundary value problem and different values of the smoothing factor k. The numerical continuation procedure is repeated as shown in Algorithm 1 until k is sufficiently high to resemble a bang-bang solution (e.g., $k_{max} = 10000$). We highlight that all of the single shooting problems are solved by a trust-region-dogleg algorithm implemented in the MATLAB function *fsolve* and for a fixed, user-defined, ToF.

5.2 Time Optimal

The goal of time optimal controller is to minimize the time of the transfer. The new cost function becomes:

$$J = \int_0^{t_f} 1 \; dt, \tag{23}$$

Algorithm 1: Summary of Continuation Approach for Fuel Optimal Solutions

Input: $\mathbf{x}_0, \mathbf{x}_f, ToF$
Result: Fuel optimal solution
Find initial adjoints with PSO for smooth problem;
Set k= 5 and solve the fuel optimal smooth problem with single shooting;
Define k_{max} = 10000;
while $k \leqslant k_{max}$ **do**
  Solve fuel optimal problem with new smoothing factor k;
  if *final state error* $\leqslant$ *max error* **then**
    Decrease control smoothing;
    Update initial adjoints;
  else
    Increase control smoothing;
  end
end
Solve fuel optimal problem with $k = k_{max}$.

implying

$$H = 1 + \boldsymbol{\lambda}_r^T \mathbf{v} + \boldsymbol{\lambda}_v^T \left(\mathbf{g}(\mathbf{r}) - 2\,[\mathbf{z}]\,\mathbf{v} + \frac{T_{max} u}{m} \boldsymbol{\alpha} \right) + - \lambda_m \frac{T_{max}}{I_{sp} g_0} u. \tag{24}$$

According to Pontryagin's minimum principle, the time optimal solution is obtained by thrusting at maximum capacity for the whole trajectory ($u(t) = 1$) along the direction of thrust dictated by primer vector theory Pan et al. (2020). The stationary conditions of the Hamiltonian return the set of ODEs shown in Equation 15 - 16 with $u = 1$. The initial and final boundary conditions are similar to the ones for the fuel optimal problem (Equation 18), except for an additional constraint on the Hamiltonian at the final time that follows from the time-free formulation of the problem Sullo et al. (2017):

$$H|_{t_f} = 0. \tag{25}$$

The solution of the time optimal problem is obtained via single shooting and MATLAB's *fsolve*. The solution of the fuel optimal problem can be exploited to obtain the initial adjoints for the time-optimal one, thereby simplifying the work of the algorithm. To this end, a solution of the fuel optimal problem that resembles the time optimal one is needed. By reducing the maximum thrust in the fuel optimal problem, the bang-bang thrust arcs are observed to increased until they almost merge into a single continuous event. The adjoints obtained at the end of this continuation procedure can be then used as initial guesses for the adjoints of the time optimal problem. Once the first solution of the time optimal is obtained a second continuation method is then introduced to bring back the thrust magnitude to the design value. A summary of this two-step continuation is offered in Algorithm 2.

5.3 Solar Sail

The last problem solved with indirect methods is the solar sail. The solar sail is a time optimal problem where the thrust is provided by solar radiation pressure acting on a reflective surface. This introduces another level of complexity if we consider that the thrust magnitude and direction would be constrained by the amount and direction of solar radiation pressure.

Recall that the normal vector of the sail ($\hat{\boldsymbol{n}}$) is defined by two

Algorithm 2: Summary of Double Continuation Approach from Fuel Optimal to Time Optimal Solutions

Input: Fuel optimal solution
Result: Time optimal solution
$T^m_{max} = 0.1 \times T_{max}$;
$\gamma = 1.1$;
$\chi = 0.95$;
$T^*_{max} = T_{max}$;
while $T^*_{max} \geqslant T^m_{max}$ **do**
  Solve Fuel Optimal problem with T^*_{max};
  if *final state error* $\leqslant$ *max error* **then**
    $T^*_{max} = T^*_{max}/\gamma$;
    update initial adjoints;
  else
    $T^*_{max} = T^*_{max}/\chi$;
  end
  if $u(t) = 1 \forall t \in [0, ToF]$ **then**
    break
  end
end
Update initial adjoints ;
while $T^*_{max} < T_{max}$ **do**
  Increase T^*_{max};
  Solve Time Optimal problem with T^*_{max};
  Update initial adjoints;
end
Solve single shooting with $T^*_{max} = T_{max}$

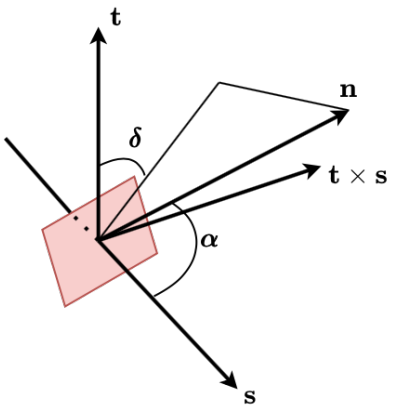

Figure 7. Solar sail directions, cone angle and clock angle

angles, the cone angle α and the clock angle δ (Fig. 7, McInnes (2004)). The cone angle is the angle between the sail normal and the sun line ($\hat{\boldsymbol{s}} = \boldsymbol{r}_1/r_1$). The clock angles is defined as the angle between the projection of the sail normal onto a plane normal to the sun line and a reference direction $\hat{\boldsymbol{t}}$. The unit vector $\hat{\boldsymbol{t}}$ is obtained by cross product of $\hat{\boldsymbol{s}}$ with $\boldsymbol{v}$, the velocity of the spacecraft:

$$\hat{\boldsymbol{t}} = \frac{\hat{\boldsymbol{s}} \times \mathbf{v}}{\|\hat{\boldsymbol{s}} \times \mathbf{v}\|}. \tag{26}$$

It follows that the components of the unit vector $\hat{\boldsymbol{n}}$ may be expressed with respect to the triad $\hat{\boldsymbol{s}}$, $\hat{\boldsymbol{w}} = \hat{\boldsymbol{t}} \times \hat{\boldsymbol{s}}$, $\hat{\boldsymbol{t}}$ as

$$\hat{\boldsymbol{n}} = \cos(\alpha)\hat{\boldsymbol{s}} + \sin(\alpha)\sin(\delta)\hat{\boldsymbol{w}} + \sin(\alpha)\cos(\delta)\hat{\boldsymbol{t}}. \tag{27}$$

The acceleration provided by the solar sail is not independent from

the state of the satellite Gong et al. (2011) and it is formulated as follow:

$$\mathbf{u} = u_{max}\left(\frac{r_{ref}}{r_1}\right)^2(\hat{\boldsymbol{s}}\cdot\hat{\boldsymbol{n}})^2\hat{\boldsymbol{n}} = \frac{\beta\mu_\odot}{r_1^2}(\hat{\boldsymbol{s}}\cdot\hat{\boldsymbol{n}})^2\hat{\boldsymbol{n}} \tag{28}$$

where r_{ref} is a reference distance used to evaluate the solar force, β is the lightness number of the sail, and $\mu_\odot = 1-\mu$ is the solar gravitational parameter . In this study the Sun-Earth distance (AU) is used as the reference distance, i.e., $r_{ref} = 1$ in normalized units.

The solar sail optimal control problem is similar to the time optimal problem in that it tries to minimize the time-of-flight between the initial and target states. However, since the solar sail does not use propellant, the mass of the spacecraft remains constant throughout the execution of the transfer. It follows that the Hamiltonian of the solar sail problem can be reformulated as:

$$\begin{aligned} H = 1 &+ \boldsymbol{\lambda}_r^T\mathbf{v} + \boldsymbol{\lambda}_v^T(\mathbf{g}(\mathbf{r}) - 2[\mathbf{z}]\mathbf{v} + \\ &+ \frac{\beta\mu_\odot}{r_1^2}(\hat{\boldsymbol{s}}\cdot\hat{\boldsymbol{n}})^2\hat{\boldsymbol{n}}). \end{aligned} \tag{29}$$

Minimizing the Hamiltonian (29) implies finding the unit vector $\hat{\boldsymbol{n}}$ that maximizes the projection of the acceleration provided by the solar sail along the primer vector $\mathbf{p} = -\frac{\boldsymbol{\lambda}_v}{\lambda_v}$. This can be obtained by minimizing:

$$\frac{\beta\mu_\odot}{r_1^2}(\hat{\boldsymbol{s}}\cdot\hat{\boldsymbol{n}})^2(\hat{\boldsymbol{n}}\cdot\boldsymbol{\lambda}_v) \tag{30}$$

or, equivalently, by maximizing

$$\frac{\beta\mu_\odot}{r_1^2}(\hat{\boldsymbol{s}}\cdot\hat{\boldsymbol{n}})^2(\hat{\boldsymbol{n}}\cdot\boldsymbol{p}). \tag{31}$$

Finally, by expressing $\boldsymbol{p}$ in the solar sail frame of Fig. 7, as

$$\boldsymbol{p} = \cos(\tilde{\alpha})\hat{\boldsymbol{s}} + \sin(\tilde{\alpha})\sin(\tilde{\delta})\hat{\boldsymbol{w}} + \sin(\tilde{\alpha})\cos(\tilde{\delta})\hat{\boldsymbol{t}}, \tag{32}$$

one finds that the optimal clock and cone angle would be given by McInnes (2004)

$$\delta^* = \tilde{\delta}, \tag{33}$$

and

$$\alpha^* = \arctan\left(\frac{-3+\operatorname{sgn}(\pi/2-\tilde{\alpha})\sqrt{9+8\tan^2(\tilde{\alpha})}}{4\tan(\tilde{\alpha})}\right), \tag{34}$$

respectively. As a result, the optimal orientation of the sail becomes

$$\hat{\boldsymbol{n}}^* = \cos(\alpha^*)\hat{\boldsymbol{s}} + \sin(\alpha^*)\sin(\alpha^*)\hat{\boldsymbol{w}} + \sin(\alpha^*)\cos(\delta^*)\hat{\boldsymbol{t}}, \tag{35}$$

which results in the adjoints dynamics given by

$$\begin{aligned} \dot{\boldsymbol{\lambda}}_r &= -G\boldsymbol{\lambda}_v + \\ &- 2\frac{\beta\mu_\odot}{r_1^3}(\hat{\boldsymbol{s}}\cdot\hat{\boldsymbol{n}}^*)(\hat{\boldsymbol{n}}^*\cdot\boldsymbol{\lambda}_v)\left(\hat{\boldsymbol{n}}^* - 2(\hat{\boldsymbol{s}}\cdot\hat{\boldsymbol{n}}^*)\hat{\boldsymbol{s}}\right), \\ \dot{\boldsymbol{\lambda}}_v &= -\boldsymbol{\lambda}_r + 2[\mathbf{z}]\boldsymbol{\lambda}_v. \end{aligned} \tag{36}$$

Similarly to the fuel and time optimal problems, the single shooting method can be applied to find optimal trajectories for the the solar sail scenario. Here, a novel homotopy procedure is implemented. The main idea is to continue from a time optimal solution to the solar sail solution by introducing a continuation parameter on the sun-line direction. Starting from the time optimal solution, it is possible to imagine a fictitious Sun-line that matches the desired direction of the primer vector. In this non-physical scenario, the time optimal and solar sail solution overlaps as long as the propellant consumption can be neglected. A continuation parameter on the Sun-line, namely $\epsilon \in [0,1]$, summarizes our approach:

$$\mathbf{s} = (1-\epsilon)\hat{\mathbf{p}} + \epsilon\hat{\mathbf{s}}. \tag{37}$$

When the ϵ parameter is 0, the sun-line moves according to the prime vector. When $\epsilon = 1$, the sun-line matches the actual location of the sun as seen from the spacecraft.

The final step is to account for the partial illumination available in the penumbra region. Here, the thrust magnitude can be modified to account for a shadow factor, $\tau(\mathbf{r})$, such that

$$\mathbf{u} = \tau\,\frac{\beta\mu_\odot}{r_1^2}(\hat{\boldsymbol{s}}\cdot\hat{\boldsymbol{n}}^*)^2\hat{\boldsymbol{n}}^*. \tag{38}$$

Next, a second continuation procedure is implemented to continue the optimal trajectory from the solar sail scenario without shadow factor to the solar sail scenario with partial illumination conditions:

$$\mathbf{u} = \left(\frac{\beta\mu_\odot}{r_1^2}(\hat{\boldsymbol{s}}\cdot\hat{\boldsymbol{n}}^*)^2\hat{\boldsymbol{n}}^*\right)(1-\eta(1-\tau)), \tag{39}$$

where η is allowed to grow from 0 to 1. The outline of our double-homotopy continuation scheme is attached in Algorithm 3.

Algorithm 3: Summary of Double Continuation Approach from Time Optimal to Solar Sail Solutions

Input: Time Optimal Solution
Result: Solar sail optimal solution
for $\epsilon = 0:1$ **do**
  single shooting solution of solar sail without shadow factor;
  update initial adjoints;
end
for $\eta = 0:1$ **do**
  single shooting solution of solar sail with shadow factor ;
  update initial adjoints;
end
single shooting solution of solar sail with shadow factor.

6 NUMERICAL SIMULATIONS

6.1 Fuel optimal

The first type of transfer that is analyzed is the fuel optimal problem with chemical propulsion for the propelled mission scenario. An optimal trajectory is first generated with the methodology of Section 5.1 and later utilized to initiate a grid search on possible combinations of time of flight and coasting time. The time of flight is varied between 10 and 30 days, whereas the coasting time to recharge the batteries after exiting the penumbra is allowed to vary between 1 and 5 days. The ΔV cost and optimal trajectories obtained with our numerical analyses are shown in Fig. 8 and 9, respectively.

It is clear that increasing the coasting time would result in higher propellant expenditures. Accordingly, the best solution found with chemical propulsion (in terms of total ΔV cost) has a coasting time in the penumbra of 1 day and a time of flight of 19.37 days. The

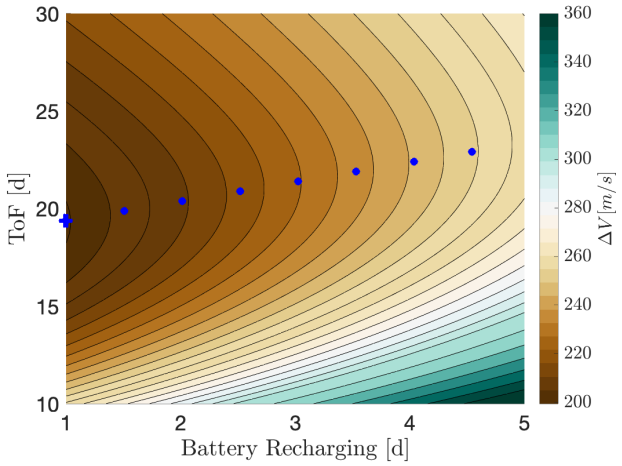

Figure 8. Fuel Optimal Chemical propulsion grid search, time for batteries recharging while coasting from the penumbra (one the x axis) and time of flight (left axis) comparison. The blue dots indicate the trajectory with the minimum fuel for a fixed coasting time.

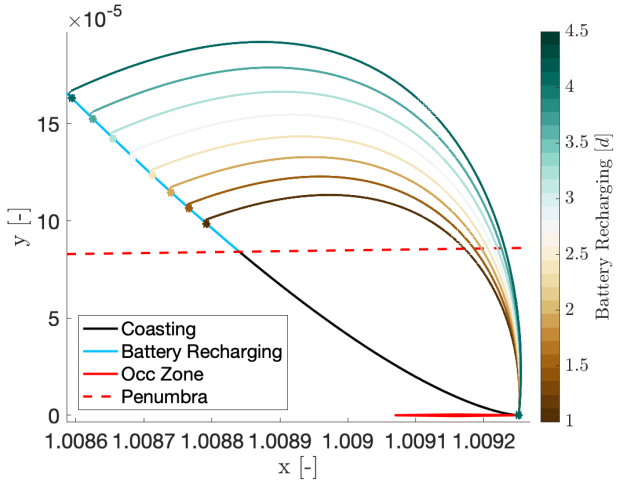

Figure 9. Fuel Optimal Grid search trajectories with chemical propulsion. The trajectories represent the blue points in Figure 8.

ΔV for one revisit is equal to 199.4 m/s, with a total cycle duration of 39.50 days (19.37 days for the controlled trajectory + 18.13 days for coasting from the occultation zone to the penumbra edge + 1 day for battery recharging + 1 day of observation). The solution presents two thrust arcs, once at the beginning and once at the end of the controlled trajectory lasting 4.77 hours and 0.50 hours respectively.

A similar simulation has been performed using low-thrust propulsion instead of chemical maneuvers (see Fig. 10 & 11). Here, the minimum fuel consumption is obtained with the smallest time of coasting (1 day) and a time-of-flight of 21.39 days; The ΔV per cycle is 213.9 m/s allowing a revisit of 24 hours every 41.52 days. The latter accounts for 18.13 days of coasting until penumbra plus one day of battery recharging and 21.39 days of transfer. As seen in the previous results with chemical propulsion, increasing the time allocated to the battery charging results in higher propellant costs. Similarly to the chemical system he solution presents two thrust arcs, once at the beginning and once at the end of the controlled trajectory lasting 53.15 hours and 5.95 hours respectively.

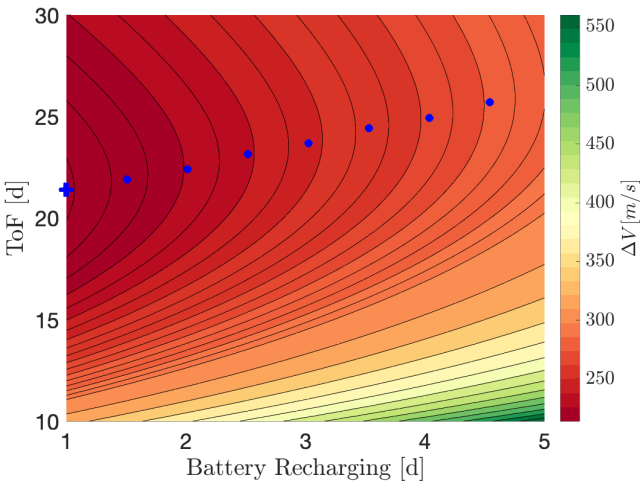

Figure 10. Fuel Optimal Low-thrust propulsion grid search, time for batteries recharging while coasting from the edge of the penumbra (one the x axis) and time of flight (left axis) comparison. The blue dots indicate the trajectories with the minimum fuel for a fixed coasting time.

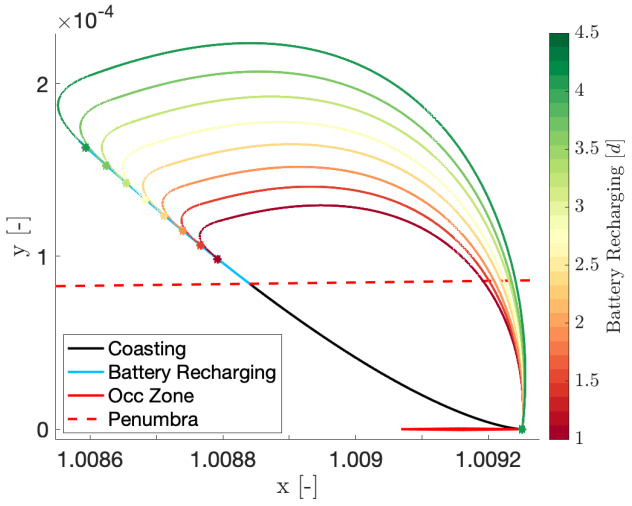

Figure 11. Fuel Optimal Grid search trajectories with low-thrust propulsion. The trajectories represent the blue points in Figure 10.

6.2 Time optimal

A grid search on the coasting time and thrust magnitude is implemented for the time optimal case. Due to higher propellant costs, chemical propulsion was not considered for time-optimal maneuvers.

For a fixed coasting time the best solution in terms of time of flight is always the one with the highest thrust. As shown in Figure 12-13, increasing the coasting time causes an increase in the time of flight similarly to the fuel optimal scenarios. The solution with the shortest time of flight of 7.43 days is obtained with the largest thrust and the shortest coasting time of 1 day. The total ΔV for this maneuver results in 652.5 m/s equivalent of propellant. The solution that requires the least amount of fuel is obtained with a maximum thrust of 0.026 N and 1 day of battery recharging, resulting in a time of flight of 19.99 days and a total ΔV of 463.6 m/s. By decreasing the maximum thrust is possible to find combinations of thrust and time for battery

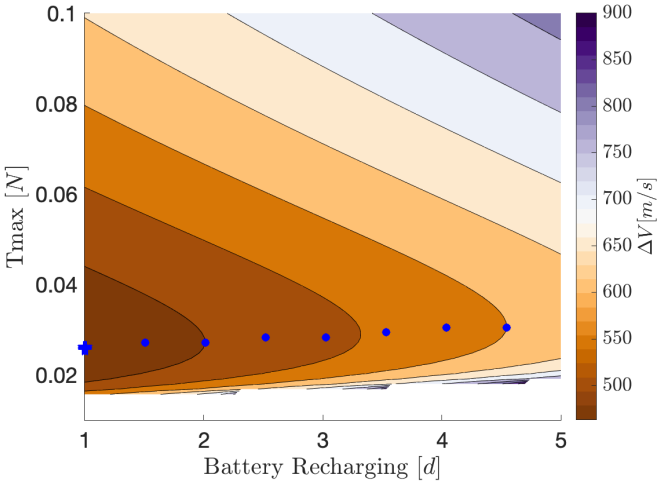

Figure 12. Time Optimal Grid search time for batteries recharging while coasting from the penumbra (one the x axis) and max thrust (left axis). The blue dots indicate the trajectory with the minimum fuel for a fixed coasting time. The white area represents combinations of acceleration and coasting time that are not feasible.

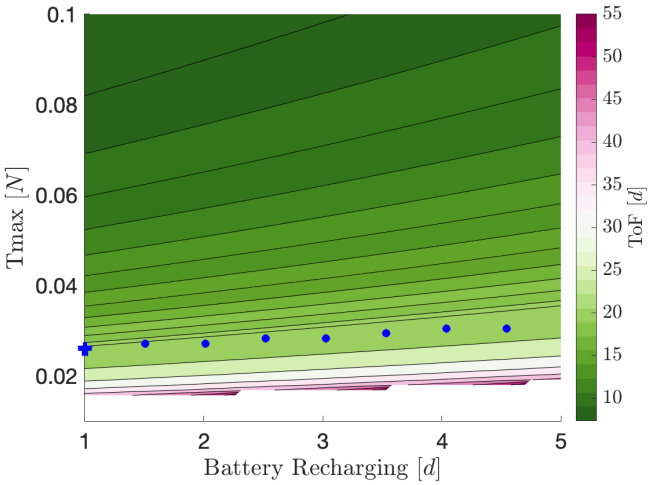

Figure 13. Time Optimal Grid search coasting time (one the x axis) and max thrust (left axis). The red dots indicate the trajectory with the minimum fuel for a fixed coasting time.

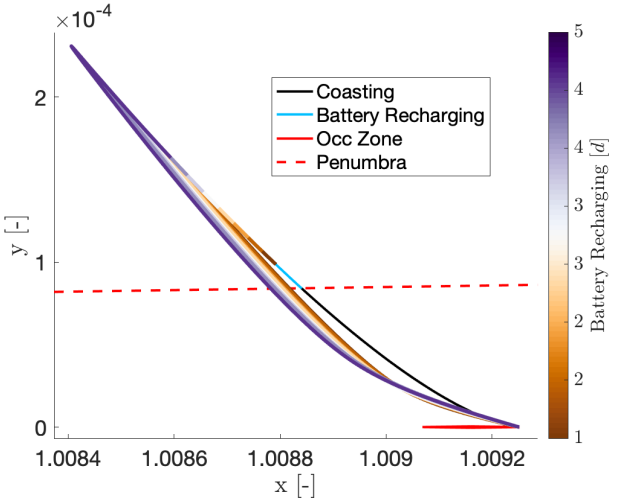

Figure 14. Time Optimal Grid search time optimal trajectories. The trajectories represent the blue points in Figure 12- 13.

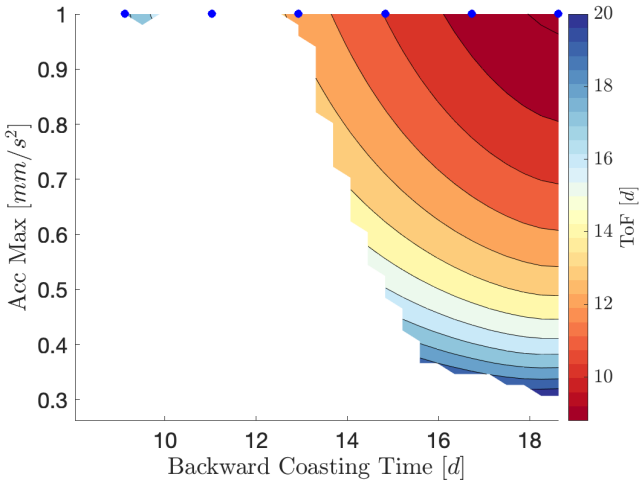

Figure 15. Solar Sail Grid search backward coasting time (from the occultation zone to the penumbra) and max acceleration (left axis). The blue dots indicate the trajectories with the minimum time for a fixed coasting time. The white area represents combinations of acceleration and coasting time that are not feasible.

recharging that do not lead to feasible combinations. These unfeasible solutions are removed from the contour plots hereafter.

6.3 Solar Sail

An interesting alternative to chemical and electric propulsion can be found in the solar sail. Due to the presence of the penumbra it is not feasible to have a solar sail solution that goes from outside the penumbra to the occultation zone as done for the propelled mission scenario. Indeed, the control capabilities of a sail would be limited by the amount of solar photons. Hence the solar sail scenario of Figure 6 is hereby considered. The initial state, $\mathbf{x}_0$, is fixed to 1 day of recharging time and the final state, $\mathbf{x}_f$, varies from the edge of the target zone to the symmetric point of $\mathbf{x}_0$ depending on the backward integration time allowed for the simulation. In this case, a grid search is performed by varying the final state and maximum acceleration of the sail.

As show in Figure 15, increasing the backward propagation time (i.e., moving away from the occultation zone) makes it easier to find feasible solutions. The minimum time of flight trajectory is obtained with the highest acceleration and the final state at the edge of the penumbra region; the lightness number found for this combination is $\beta = 0.169$, corresponding to a sail loading of 9.08 g/m^2. However choosing a final state at the edge of the penumbra means longer cycles due to the required coasting time to go from $\mathbf{x}_f$ to the occultation zone. It follows that the solution with the shortest time of flight is not necessary the best in terms of number of observations.

Figure 16 illustrates solutions according to the time elapsed between two consecutive observations. The best case is observed with a backward coasting of 12.93 days and a maximum acceleration of 1 mm/s^2. The length of the cycle is found to be 44.76 days as opposed

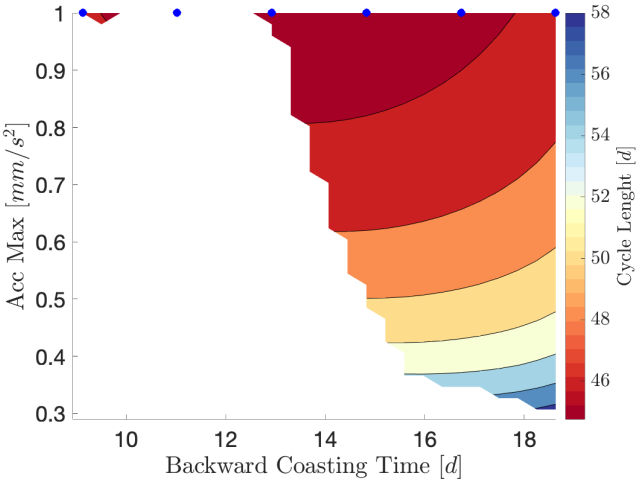

Figure 16. Solar Sail Grid search backward coasting time (from the occultation zone to the penumbra) and max acceleration (left axis). The white area represents combinations of acceleration and coasting time that are not feasible.

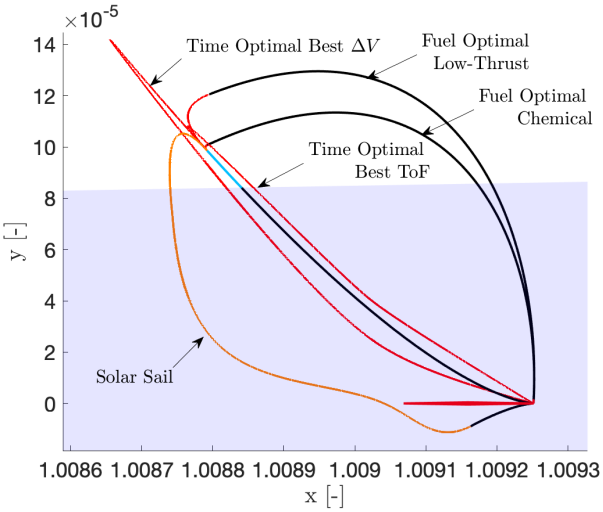

Figure 18. Trajectories of the best solutions for Fuel Optimal, Time Optimal and Solar Sail. The red part of the trajectory represents where the engine is on, cyan represents the battery recharging and black the coasting arcs. For the solar sail there is no thrust arc.

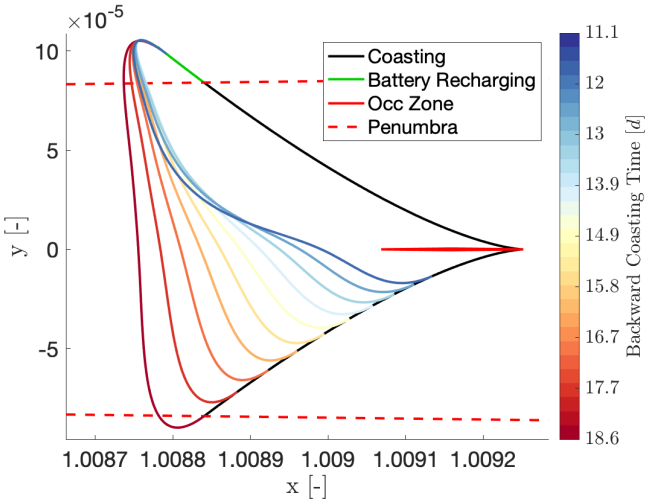

Figure 17. Solar Sail Grid search optimal trajectories. The trajectories represent the blue points in Figure 15.

to 27.56 days obtained from the minimum time-of-flight trajectory. In Figure 15 it is shown that feasible solutions exists by adopting smaller values of maximum acceleration that the nominal case of 1 mm/s^2; the lowest values of acceleration for which a feasible solution is found 0.306 mm/s^2 and the corresponding to a lightness number of 0.05175.

7 COMPARISON AND DISCUSSION

Some final considerations can be drawn from the previous simulations and results as summarized in Table 3 - 4. The time optimal with the best time-of-flight solution allows to decrease the time between subsequent observations while using 3 times less propellant than chemically propelled trajectories. As expected the time optimal solution is less efficient in terms of ΔV when compared to fuel optimal low-thrust trajectory, as the second one requires a third of the fuel at the expenses of a higher time-of-flight; a trade-off between revisit times and fuel consumption has to be performed. Chemical propulsion enables to achieve similar transfers with a lower ΔV consumption when compared to low-thrust technologies. However, since the specific impulse of the chemical engine is smaller, the required fuel mass can be more than 10 times larger than the one required for low-thrust. The chemical option remains interesting; in particular, if few observations are required, chemical propulsion should be considered due to lower complexities and far less stringent power requirements. The low-thrust option seems to be preferable in terms of propellant costs, even though the overall system mass of the thruster should be taken into account to draw final conclusions. The type of thruster that is analyzed falls into the category of Hall engines. These type of low-thrust engines tend to be more demanding from a system power point of view than another low-thrust systems. Nevertheless, as highlighted in the time optimal solutions of Figure 12, it is possible to find feasible solutions with lower thrust values. As Hall thrusters have the advantage of being adaptable over a wide range of power levels Krejci & Lozano (2018), it seems possible to mitigate power requirements by considering different thrust value (see, for example, the time optimal low-thrust best ΔV reported in Table 3). Nevertheless, we highlight that the second burn maneuver in the propelled mission scenario is always occurring within the penumbra region of the Sun-Earth system (see, e.g., Figure 18). The situation gets worse when considering time-optimal trajectories where the satellite constantly thrusts while passing through the penumbra and umbra regions. Batteries should be sized accordingly in order to provide the power required for the burning arcs, and this can quickly escalate to impractical system designs. In the case of fuel optimal solutions is possible to take advantage of the coasting arcs after the first burn arc to recharge the batteries. The coasting arc outside the penumbra region for the chemical represents 55.3% (10 days) of the whole coasting arc while for the low-thrust solution the 64.5% (13.6 days).

As an alternative, it is possible to consider fuel and time-optimal trajectories in the solar sail scenario where the state of the spacecraft is propagated backwards until it leaves the penumbra region of the Sun-Earth system. For instance, consider the case where the final

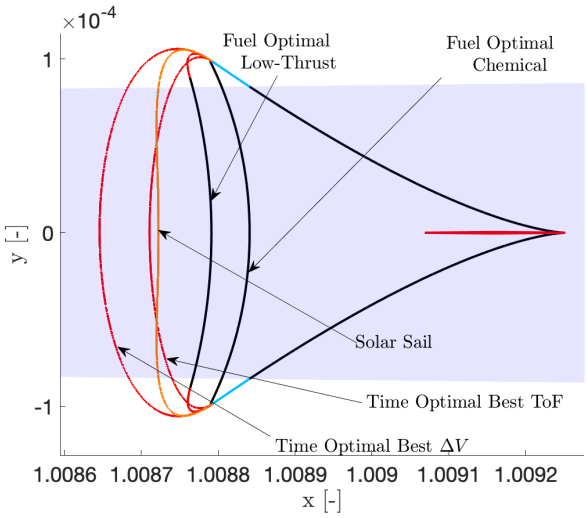

Figure 19. Trajectories of the best solutions for Fuel Optimal, Time Optimal and Solar Sail for the solar sail scenario with symmetric initial and final conditions. The red part of the trajectory represents where the engine is on, cyan represents the battery recharging and black the coasting arcs. For the solar sail there is no thrust arc.

state, $\mathbf{x}_f$, is chosen to be the symmetric of the initial state, $\mathbf{x}_0$, with respect to x-axis of the synodic frame.

As shown in Figure 19, battery recharging would take place before and after the end of the transfer phase, thereby relaxing potential system engineering constraints. However, if the focus is given only on ΔV and time-of-flight, fuel optimal solutions with this mission profile do not seem to give any advantage when compared with optimal trajectories from the propelled mission scenario. This is not the case for time optimal trajectories, which showcase a slight improvement in terms of total ΔV costs. As summarized in Table 4, the length of a cycle increases when compared to the time optimal transfer of the nominal mission scenario due to the fact that in the solar sail scenario the coasting time is basically doubled. The results from the nominal mission scenario appears to be more efficient than the symmetric solar sail scenario in terms of time elapsed between consecutive observations. Nevertheless, batteries requirements could be relaxed by using a symmetric solar sail scenario. Decreasing the battery size would mean decreasing the overall weight and therefore cost of the mission. Alternatively, more fuel could be stored on-board to enable more measurement campaigns and improve upon the scientific output of the mission.

Transfers in the solar sail scenario are the only options for solar sail solutions. In fact the solar sail solutions cannot reach the occultation zone due to the decrease of solar radiation pressure in the last phase of the transfer. We highlight that the solar sail scenario could provide longer mission duration as there are practically no constraints due to fuel consumption. However, prohibitive area-to-mass ratios can quickly make the solar sail configuration the most unfeasible among the propulsion systems being analyzed for this work. Indeed, the values obtained for the optimal solar sail solution are still quite far from existing solar sail missions. Lightsail 2, for example, has a lightness number of 0.009799, i.e., 5 to 17 times smaller than the lightness numbers identified in Section 6.3 Spencer et al. (2020). Future work will assess the feasibility of designing solar sail transfers that would avoid the penumbra region and operate at more realistic lightness numbers.

8 CONCLUSION

In this paper a feasibility analysis was performed for a novel sun occultation mission that uses the Earth as a natural occulter. The occultation provided by the Earth would enable more frequent and longer observations of the Sun corona than the one performed on the ground during total eclipses. Focus was given to optimal trajectories that bring the spacecraft back into the Earth occultation zone via either chemical propulsion, low-thrust technologies, or solar sailing. Fuel, time, and solar sail optimal control problems were solved via indirect optimization techniques. To deal with the small convergence radius of the single shooting method, various continuation procedures were implemented. A new continuation method on the sun-line was hereby introduced to robustly pass from the time optimal solution to the solar sail solution.

Grid search analyses revealed that fuel optimal trajectories with both chemical and low-thrust propulsion could be compatible with a small satellite mission (100–500 kg). The ΔV consumption per cycle was found to be 199 m/s and 213 m/s, with chemical and electric propulsion, respectively. This propellant cost is relatively small if compared to the ΔV equivalent of time optimal solutions. Nevertheless, time optimal solutions displayed shorter revisit times between consecutive observations, making them an interesting alternative for shorter mission life cycles.

Solar sail solutions are possible and competitive when compared to traditional propulsion systems due to virtually zero-propellant costs. However, we highlight that area-to-mass ratios can quickly become impractical from a technological point view. More research is warranted in order to validate the feasibility of a solar-sail design with lightness numbers in the range of $\beta \in [0.0098, 0.01]$. Future work will consider fully sunlit transfers that avoid the penumbra region and explore the feasibility of lower lightness numbers. In parallel to this, future research will focus on adopting a more accurate dynamical model, taking into account the Earth's elliptic orbit and seasonal effects on the observations given by Earth's oblateness. More focus will be given to addressing possible issues in the observations produced by atmospheric refraction.

ACKNOWLEDGEMENTS

The authors would like to thank former MSc students Sadia Sarker, Phil Holding, Alexandru Uifălean, and Homiros Papadatos-Vasilakis for their contributions to this topic.

DATA AVAILABILITY

The inclusion of a Data Availability Statement is a requirement for articles published in MNRAS. Data Availability Statements provide a standardised format for readers to understand the availability of data underlying the research results described in the article. The statement may refer to original data generated in the course of the study or to third-party data analysed in the article. The statement should describe and provide means of access, where possible, by linking to the data or providing the required accession numbers for the relevant databases or DOIs.

REFERENCES

Altschuler M. D., Newkirk G., 1969, Sol. Phys., 9, 131
Arnaud J., Newkirk G. J., 1987, A&A, 178, 263

Type of Transfer	Δv per Cycle	Max Acc	Mass of Fuel per Cycle	Time of Flight	Length of a Cycle	Mission Scenario
Fuel Optimal Chemical	199.44 m/s	$10^{-2} m/s^2$	9.67 kg	19.37 d	39.50 d	Propelled
Fuel Optimal Low-Thrust	213.95 m/s	$10^{-3} m/s^2$	1.08 kg	21.39 d	41.52 d	Propelled
Time Optimal Low-Thrust Best ToF	652.50 m/s	$10^{-3} m/s^2$	3.27 kg	7.43 d	27.55969 d	Propelled
Time Optimal Low-Thrust Best ΔV	463.6 m/s	$0.26 \times 10^{-3} m/s^2$	2.34 kg	19.99 d	40.12 d	Propelled
Solar Sail	n/a	$10^{-3} m/s^2$	n/a	12.93 d	44.76 d	Solar Sail

Table 3. Best solutions for the two mission scenarios

Type of Transfer	Δv per Cycle	Max Acc	Mass of Fuel per Cycle	Time of Flight	Length of a Cycle
Fuel Optimal Chemical	274.50 m/s	$10^{-2} m/s^2$	13.06 kg	10 d	49.26 d
Fuel Optimal Low-Thrust	289.64 m/s	$10^{-3} m/s^2$	1.46 kg	10.22 d	49.49 d
Time Optimal Low-Thrust Best ToF	431.95 m/s	$10^{-3} m/s^2$	2.18 kg	4.94 d	44.21 d
Time Optimal Low-Thrust Best ΔV	349.83 m/s	$0.4 \times 10^{-3} m/s^2$	1.77 kg	10.03 d	49.29 d
Solar Sail	n/a	$10^{-3} m/s^2$	n/a	8.97 d	48.23 d

Table 4. Best Solutions for the symmetric solar sail scenario.

Boe B., Habbal S., Druckmüller M., 2020, The Astrophysical Journal, 895, 123

Conway B. A., 2010, Spacecraft Trajectory Optimization. Cambridge Aerospace Series, Cambridge University Press, doi:10.1017/CBO9780511778025

Domingo V., Fleck B., Poland A. I., 1995, Solar Physics, 162, 1

Eckersley S., Kemble S., 2017, Method of solar occultation, https://patents.google.com/patent/EP2641833B1/en

Erdelyi R., 2019, HiRISE - High Resolution Imaging and Spectroscopy Explorer Ultrahigh resolution, interferometric and external occulting coronagraphic science: Great leap in solar physics, https://www.cosmos.esa.int/web/voyage-2050/white-papers

Gong S.-P., Gao Y.-F., Li J.-F., 2011, Research in Astronomy and Astrophysics, 11, 981

Jiang F., Baoyin H., Li J., 2012, Journal of guidance, control, and dynamics, 35, 245

Koon W. S., Lo M. W., Marsden J. E., Ross S. D., 2008, Free online Copy: Marsden Books

Krejci D., Lozano P., 2018, Proceedings of the IEEE, 106, 362

Landi E., Hutton R., Brage T., Li W., 2020, ApJ, 904, 87

Lin H., Kuhn J. R., Coulter R., 2004, ApJ, 613, L177

Llorente J. S., Agenjo A., Carrascosa C., de Negueruela C., Mestreau-Garreau A., Cropp A., Santovincenzo A., 2013, Acta Astronautica, 82, 38

Loreggia D., et al., 2019, in 2019 IEEE 5th International Workshop on Metrology for AeroSpace (MetroAeroSpace). pp 484–489

Lyot B., 1932, Z. Astrophys., 5, 73

MacQueen R. M., Csoeke-Poeckh A., Hildner E., House L., Reynolds R., Stanger A., Tepoel H., Wagner W., 1980, Sol. Phys., 65, 91

McInnes C. R., 2004, Solar sailing: technology, dynamics and mission applications. Springer Science & Business Media

Montenbruck O., Gill E., Lutze F., 2002, Appl. Mech. Rev., 55, B27

Pan X., Pan B., Li Z., 2020, The Journal of the Astronautical Sciences, 67, 1220

Rasotto M., Armellin R., Di Lizia P., 2016, Engineering Optimization, 48, 519

Schatten K. H., Wilcox J. M., Ness N. F., 1969, Sol. Phys., 6, 442

Si R., Brage T., Li W., Grumer J., Li M., Hutton R., 2020, ApJ, 898, L34

Spencer D. A., Betts B., Bellardo J. M., Diaz A., Plante B., Mansell J. R., 2020, Advances in Space Research

Sullo N., Peloni A., Ceriotti M., 2017, Journal of Guidance Control Dynamics, 40, 2796

Tomczyk S., McIntosh S. W., Keil S. L., Judge P. G., Schad T., Seeley D. H., Edmondson J., 2007, Science, 317, 1192

Zouganelis I., et al., 2020, A&A, 642, A3

This paper has been typeset from a TEX/LATEX file prepared by the author.